MRS Advances

Hybrid improper antiferroelectricity—New insights for novel device concepts

Xue-Zeng Lu and James M. Rondinelli

Department of Materials Science and Engineering, Northwestern University, Evanston, Illinois 60208, USA

Correspondence Email: xuezeng.lu@northwestern.edu

Abstract

Antiferroelectrics have been studied for decades, with most research focused on $PbZrO_3$ or related compounds obtained through chemical substitution. Although there are several important antiferroelectrics found in AVO_4 (A=Dy, Bi), orthorhombic ABC semiconductors (e.g., MgSrSi) and hydrogen-bonded antiferroelectric materials, experimentally demonstrated antiferroelectrics are far less common. Furthermore, antiferroelectrics have potential applications in energy storage and for strain and force generators. In recent years, hybrid improper ferroelectrics have been intensively studied, along which the hybrid improper antiferroelectric phase was proposed and demonstrated in (001) Ruddlesden−Popper $A_3B_2O_7$ thin films from first-principles calculations. Later, the hybrid improper antiferroelectric phase was discovered experimentally in several Ruddlesden−Popper perovskites in bulk. Across the hybrid improper ferroelectric-antiferroelectric phase transition, several interesting phenomena were also predicted. In this snapshot review, we describe recent progress in hybrid improper antiferroelectricity.

INTRODUCTION

In the early definition of an antiferroelectric material [1], there is a nonpolar mode that condenses in the paraelectric phase and there is an anomalous dielectric response at the critical antiferroelectric transition temperature. Moreover, there will be an induced ferroelectric phase after applying an electric field [2]. In terms of the Landau-model expansion, in an antiferroelectric structure with two (or more) well-defined sublattices, the polarizations among the sublattices are antialigned, which can be aligned

to produce a polar phase by applying electric field [3]. A recent proposed criterion for determining whether a nonpolar centrosymmetric structure is an antiferroelectric phase relies on a symmetry analysis [4]: an antiferroelectric phase should exhibit a symmorphic polar subgroup that preserves the polar sites of the antiferroelectric phase. In antiferroelectric materials, the antiferroelectric phase is the ground state structure, while the antiferroelectric phase may also exist in ferroelectric materials as an intermediate phase over a finite temperature range. Therefore, finding the antiferroelectric phase should be very important. Compared with ferroelectric materials, researchers have focused less on antiferroelectric materials, perhaps because no macroscopic electric field couples to the nonpolar mode, which limits potential functionalities. Furthermore, antiferroelectric materials/phase demonstrated in experiments are challenging and have been limited to date [5].

From the above definition, the relation between ferroelectricity and antiferroelectricity can be analogous to that between ferromagnetism and antiferromagnetism. Yet, ferroelectric oxides, for example, are far more common than the antiferroelectric oxides. In contrast, there are many antiferromagnet oxides and few ferromagnetic oxides. The well-defined antiferroelectric materials are $PbZrO_3$ and $PbZrO_3$-based materials (ion substitution) [6,7], AVO_4 (*A*=Dy, Bi) [8], orthorhombic *ABC* semiconductors (e.g., MgSrSi) [9] and hydrogen-bonded antiferroelectric materials [10-13]. In $PbZrO_3$, the high-temperature phase exhibits a paraelectric cubic ideal perovskite structure ($Pm\bar{3}m$) and the phase is transformed to an orthorhombic distorted perovskite structure (*Pbam*) at 505K [14]. This phase transition was demonstrated to be an antiferroelectric phase transition and the *Pbam* structure is antiferroelectric. The possible ferroelectric phases, which may be obtained by applying the electric field along the principle axis *x* (*y* or *z*) and along the diagonal axis *xy* (*yz* or *xz*), are *P*4*mm* and *Amm*2, respectively [4]. Then, from a Landau model [4] and careful experimentation [15], a double hysteresis loop was found, which confirmed the antiferroelectric transition in $PbZrO_3$.

Although few materials have been shown to be antiferroelectric or exhibit an antiferroelectric phase at at a finite temperature, these materials can host functionalities of potential technological interest. For example, the direct consequence of a ferroelectric-to-antiferroelectic transition is the ability to control the polarization from a non-zero value to null, and activation of relevant polar noncentrosymmetric functionalities The phase transition will also result in a spontaneous strain, which can be used for strain and force generators and electrostrictive elments. Furthermore, the double hysteresis loop can lead to a large capacitive storage application [4].

In studies of $n = 2$ Ruddlesden–Popper (RP) $A_3B_2O_7$ compounds, researchers have shown a nonpolar *Pbcn* phase is stabilized under tensile strain in $Ca_3Ti_2O_7$ (001) thin films, which induces a polar-to-nonpolar phase transition [16]. The polar phase exhibits $Cmc2_1$ symmetry [17-21], which leads to hybrid improper ferroelectricity (HIF) that is similar to that proposed in $YMnO_3$ [22] and $PbTiO_3/SrTiO_3$ heterostructures [23]. In the $Cmc2_1$ phase (see **Figure 1**), there are polar ($Q_{\Gamma_5^-}$), oxygen octahedral *rotation* (OOR) ($Q_{X_2^+}$), and oxygen octahedral *tilt* (OOT) ($Q_{X_3^-}$) modes, which couple through a trilinear interaction, $Q_{\Gamma_5^-}Q_{X_2^+}Q_{X_3^-}$, to stabilize the polar ground state structure and lead to the functional electric polarization $P \propto Q_{X_2^+}Q_{X_3^-}$. Later, hybrid improper ferroelectric materials attracted considerable attention, especially, after the experimental demonstration of hybrid improper ferroelectricity in $Ca_3B_2O_7$ (*B*=Mn,Ti) compounds [24-26]. Although remarkable functionalities were proposed to occur along with the hybrid improper ferroelectricity, a limited number of new demonstrations have been made owing to the complexity of switching.

Compared to hybrid improper ferroelectricity, the *Pbcn* phase was proposed [12,27] and discovered in very recent experiments [28,29]. This *Pbcn* phase is a hybrid

improper *antiferroelectric* phase, since the nonpolar mode ($Q_{M_5^+}$) is also induced by two zone-boundary modes [e.g., oxygen octahedral *rotation* ($Q_{X_1^-}$) and oxygen octahedral *tilt* ($Q_{X_3^-}$)] through a trilinear coupling interaction $Q_{M_5^+}Q_{X_1^-}Q_{X_3^-}$. Furthermore, an antiferroelectric phase can be universal in thin films of any compounds exhibiting geometric ferroelectricity (e.g., trilinear couplings) [30]. This idea was demonstrated recently in $A_3B_2O_7$, ABO_3/$A'BO_3$ and $AA'BB'O_6$ compounds. Then, several interesting phenomena were enabled by transitions between the hybrid improper ferroelectric and antiferroelectic phases, including tunable dielectric responses across the transition [16]; tunable weak ferromagnetism along with the transition [27]; and an indirect band gap to direct band gap transition along the transition [30]. Moreover, the antiferroelectric phase is also helpful for understanding the polarization switching behaviors and topological defects in the domain walls of the *n*=2 Ruddlesden–Popper compounds.

The above phenomena are new or rarely studied and the transition between hybrid improper ferroelectricity and antiferroelecticity can lead to functionalities that may be exploited for spintronic devices and optical materials [27,30].In this snapshot review, we first discuss several (hybrid improper) antiferroelectric phases in *n*=2 Ruddlesden–Popper compounds. Then, we show how the hybrid improper ferroelectric and antiferroelectic phase transition imparta tunable functionalities and plays an important role in the domain walls of antiferroelectrics. Last, we discuss future opportunities for hybrid improper antiferroelecticity.

HYBRID IMPROPER ANTIFERROELECTRIC *Pbcn* PHASE IN $A_3B_2O_7$

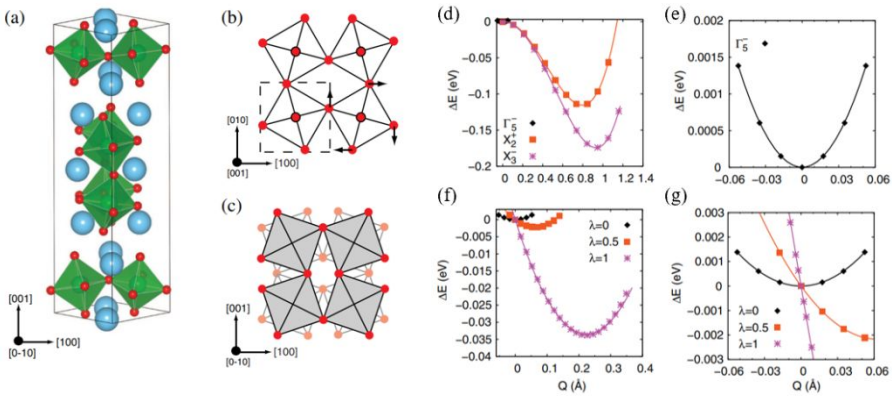

Figure 1. (a) The *Cmc*2_1 ferroelectric ground state structure of $Ca_3Mn_2O_7$. The large (blue) spheres are Ca ions. (b) The schematic illustration of the atomic displacements corresponding to the X_2^+ (Q_R) rotation in which the dashed square displays the unit cell of the *I*4/*mmm* high-symmetry structure. (c) The X_3^- (Q_T) tilt mode. The coordinate system is that of the *I*4/*mmm* high-symmetry structure. (d) The mode energy with changing the amplitude of the mode. (e) The enlargement of figure (d) in an energy range above 0eV for Γ_5^- polar mode. (f) The energy dependence on the amplitude of $\lambda \sim Q_{X_2^+}Q_{X_3^-}$, where Q represents the amplitude of a phonon mode. (g) The enlargement of figure (f) in an energy range around 0 eV. Figures reproduced from Ref. 17, Copyright American Physical Society, 2011.

$A_3B_2O_7$ compound consists of two ABO_3 perovskite blocks stacked along the $[001]_{pt}$ pseudo-tetragonal (pt) direction that are separated by a rock salt AO layer every two 5-atom perovskite unit cells. Importantly, in the ground state phase of *Cmc*2_1 symmetry, there are two oxygen octahedral rotations (OORs), which are the *in-phase*

OOR ($Q_{X_2^+}$) about the) $[001]_{pt}$ direction and the OOT ($Q_{X_3^-}$) occurs about the $[\bar{1}10]_{pt}$ direction, respectively (see **Figures 1a-1c**). They are also the primary distortion modes (i.e., the most unstable distortion modes appearing in the ideal *I*4/*mmm* structure) governing the polar ground state phase in these layered $A_3B_2O_7$ materials [17-21] (see **Figures 1d and 1e**). Then, a polar mode ($Q_{\Gamma_5^-}$) appears through the so-called trilinear coupling ($Q_{\Gamma_5^-}Q_{X_2^+}Q_{X_3^-}$) in the *Cmc*2$_1$ phase, which should not be condensed by itself because of its positive phonon mode frequency (see **Figures 1f and 1g**). Furthermore, this polar phase is often the bulk ground state phase in many $A_3B_2O_7$ compounds and $A_3B_2O_7$-based compounds (A-site or B-site ion substitution) with a small tolerance factors, e.g., τ <1 [20,24-26,31] (see **Figure 2**). The tolerance factor is defined as $\tau = \frac{r_A + r_O}{\sqrt{2}(r_B + r_O)}$, where r_A, r_B and r_O are the radii of the A, B cations and oxide anion, respectively, which has been used as a descriptor for octahedral rotation stability in the layered $A_3B_2O_7$ compounds [16]. More intriguingly, the HIF was confirmed by very recent experiments in $(Ca,Sr)_3Ti_2O_7$ single crystals [24], $Ca_3Ti_2O_7$ and $Ca_3Mn_2O_7$ polycrystalline crystals [25], $Ca_3(Ti,Mn)_2O_7$ ceramics [26], $Sr_3Zr_2O_7$ [28] and $Sr_3Sn_2O_7$ [29,32] compounds. In $(Ca,Sr)_3Ti_2O_7$ single crystals, the authors also showed the existence of the switchable *P* with a low coercive electric field.

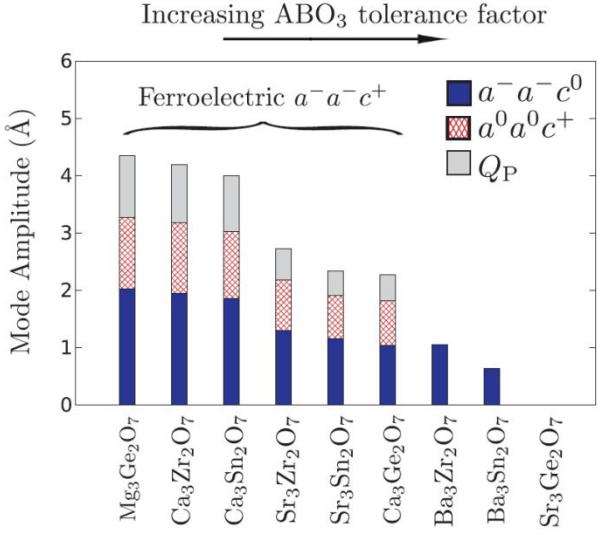

Figure 2. Mode decompositions in $A_3B_2O_7$ oxides as a function of tolerance factors. Figure reproduced from Ref. 20, Copyright WILEY-VCH Verlag GmbH & Co. KGaA, Weinheim, 2013.

Epitaxial strain engineering is a powerful tool to generate and tailor the functionalities in thin films of complex oxides (e.g., ABO_3 perovskites). The strain imposed by the substrate can affect all – polar, OOR and OOT – modes involved in stabilizing the ferroelectric phase. For example, on the one hand, ferroelectricity can be produced and enhanced in the film relative to the bulk counterpart, due to the strong coupling between the strain and polarization (see Ref. [33] and papers therein). On the other hand, owing to the strong coupling of the oxygen octahedral rotations to the strain [34], the amplitude and pattern of the OOR and OOT will also be influenced.

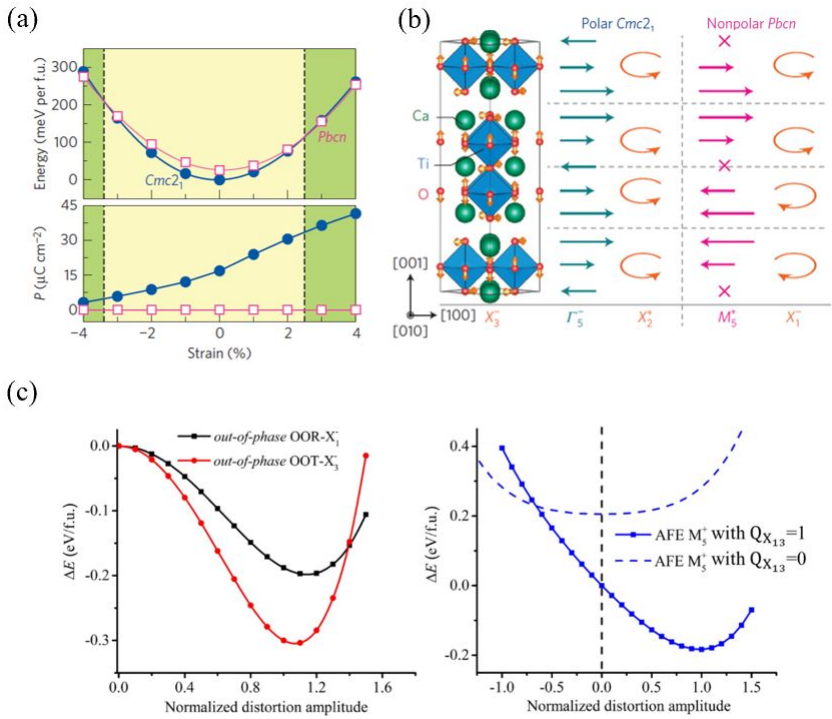

Figure 3. (a) Top: The calculated total energies as a function of epitaxial strain in the strain range of -4 – 4%, where ΔE is the energy difference relative to the energy of $Cmc2_1$ phase at 0% strain. Bottom: Polarization as a function of strain in each phase. (b) Illustration of the distortion modes in $Cmc2_1$ and *Pbcn* phases with respect to the high-symmetry *I*4/*mmm* reference structure. The structure (left) shows the double-layered RP structure with two-dimensional layers of corner-connected TiO_6 polyhedra in the *I*4/*mmm* symmetry. The arrows on the oxide ions indicate the displacement pattern for the out-of-phase OOT about $[\bar{1}10]$, which transforms as irrep X_3^-. The displacement modes described by irreps Γ_5^- and M_5^+ induce layer resolved polarizations *P*, with the direction and magnitude indicated schematically by the blue arrows. Note that irreps Γ_5^- (M_5^+) produces (no) macroscopic electric polarization, and the cross in M_5^+ indicates that *P*=0 μC cm^{-2} in that layer. (c) Energy versus the normalized magnitudes of X_1^-, X_3^- and M_5^+ distortions at 0% strain. Here the *I*4/*mmm* structure is treated as the reference structure. ΔE is the energy difference relative to the energy at zero mode amplitude. The normalizations for X_1^-, X_3^- and M_5^+ distortions are made with respect to the magnitudes of X_1^-, X_3^- and M_5^+ distortions in the *Pbcn* structure at 0% strain, respectively. In the right panel, $Q_{X_{13}}$~$Q_{X_1^-}Q_{X_3^-}$. The change in the OOR rotation sense, i.e., appearance of the $Q_{X_1^-}$ OOR mode combined with the $Q_{X_3^-}$ OOT mode, activates the AFE $Q_{M_5^+}$ mode displacements and stabilizes the nonpolar *Pbcn* phase. Figures reproduced from Ref. 16, Copyright Springer Nature, 2016.

A genetic algorithm (GA) structural search method was adopted to obtain a new phase under both compressive and tensile strain in the (001) strained $Ca_3Ti_2O_7$ [16]. The $Cmc2_1$ ground state phase was also produced in the GA search in bulk and at 0% strain. The new phase has a nonpolar *Pbcn* symmetry, which is a lower-energy metastable structure compared to the bulk. This *Pbcn* phase should be antiferroelectric, because there is a polar site "1", which can be preserved in the symmorphic polar subgroup of *Pbcn* phase, that is the *P*1 phase. The computed energy versus strain diagram using density functional theory (DFT) calculations and the Perdew-Burke-Ernzerhof revised for solids (PBEsol) functional [35] showed that the critical compressive and tensile

strains are -3.3% and 2.6%, respectively (see **Figure 3a**). These polar-to-nonpolar (P-NP) phase transitions at both compressive and tensile strains are unusual in (001) thin films, because the compressive strain and tensile strain in the (001) thin film favor *out-of-plane* polarization and *in-plane* polarizations, respectively, as well demonstrated in many previous experimental and computational studies [33]. But here, large strain was identified to suppress the polarization, making it zero at the transition.

The phase transitions at both compressive and tensile strains exhibit changes of the OOR mode, which are *in-phase* OOR in $Cmc2_1$ and *out-of-phase* OOR ($Q_{X_1^-}$) in *Pbcn* (see **Figure 3b**). Because both phases have an *out-of-phase* OOT ($Q_{X_3^-}$) mode, the change of the OOR rotational sense results in the change between the polar mode and nonpolar mode ($Q_{M_5^+}$) that has a positive mode frequency. In the *Pbcn* phase, the nonpolar mode is induced by the coupled OOR and OOT modes through a trilinear coupling ($Q_{M_5^+} Q_{X_1^-} Q_{X_3^-}$) (see **Figure 3c**).

$$E=E_0+\alpha_i Q_i^2 + \beta_i Q_i^4 + \alpha_j Q_j^2 + \beta_j Q_j^4 + \alpha_k Q_k^2 + \beta_k Q_k^4 + h_{i0} Q_i Q_j Q_k + h_{i1} Q_i Q_k Q_j^3 + h_{i2} Q_i Q_j Q_k^3 + \gamma_{ij} Q_i^2 Q_j^2 + \gamma_{jk} Q_j^2 Q_k^2 + \gamma_{ik} Q_i^2 Q_k^2$$

By using a phenomenological Landau model, the phase diagram under strain was obtained and compared with that directly obtained from DFT calculations. The results showed good agreement between the two methods (see **Figure 4a**). In the Landau model, E_0 is the energy of the *I*4/*mmm* structure, Q_i, Q_j and Q_k represent the order parameters with amplitudes in units of Å for the FE [antiferroelectric (AFE)] [i=Γ_5^- (M_5^+)], in-phase OOR (out-of-phase OOR) [j=X_2^+ (X_1^-)] and OOT (k=X_3^-) distortions in $Cmc2_1$ (*Pbcn*), respectively, and $\alpha_{i,j,k}$, $\beta_{i,j,k}$, h_{i0}, h_{i1}, h_{i2} and $\gamma_{ij,jk,ik}$ are the corresponding coefficients. It should be noted that to obtain the phase diagram appearing in Fig. 4(a), the Landau phenomenological expansion was minimized at each strain value by directly carrying out the DFT calculations rather than fitting the coefficients in the expansion. Here the in-plane lattice constant and the normalized Q modes (obtained by using group-theory analysis [16]) considered in equation are constrained, that is, the magnitude of the order parameter is equal to unity and the order parameter direction is also fixed, however, the internal atomic positions are allowed to be optimized according to the directions of the Q modes considered (that is, the magnitude of Q is relaxed in the optimization) and the *c*-lattice constant is also optimized. This allows us to efficiently and accurately obtain the total energies. Note that this method then leads to the Γ_1^+ mode, which contains the full symmetry of *I*4/*mmm*, being omitted in the Landau equation and therefore excluded from Fig. 4. This difference leads to the small variation in the strain phase stability diagrams compared with the one directly obtained from DFT calculations. Also, if using the Landau model with fitting coefficients, the quality of the obtained phase diagram will be correlated to the terms that are included in the model. If there are a few terms (less than 4th order) in the model, the quality will be bad for $Ca_3Ti_2O_7$ in our study, while the expansion up to 5th order is better. But there must be some discrepancies by using the Landau model with the fitting coefficients. In our method above, the direct DFT calculations based on the Landau model can include all the terms related to each mode included in the Landau mode, then the accuracy is enhanced significantly. As mentioned earlier that the Γ_1^+ mode is ignored, which is usually done in the Landau model expansion, there is still discrepancy that needs to be verified to be small.

Then, the energy terms purely comprised of antiferrodistortive (AFD) modes (i.e., OOR and OOT modes) and the energy terms including the interactions between the polar (nonpolar) mode and the AFD modes were isolated. The energy terms including the

pure polar (nonpolar) mode are also included in the latter contribution in this decomposition, which is broadly referred to as "trilinear-related coupling terms," because it contains the important trilinear-related terms that significantly contribute to phase stability. Although the total effects of the two contributions can lead to the P-NP transition, there is no phase transition in each contribution (see **Figures 4a-4c**). Moreover, the AFD contribution decreases with increasing tensile strain (see **Figure 4b**), while the trilinear-related coupling terms increase with increasing tensile strain (see **Figure 4c**). In addition, the AFD energy contribution in the nonpolar phase is larger than that of polar phase; the trilinear-related coupling terms in nonpolar phase is smaller than that of polar phase. From this analysis, it was deduced that the strong competing of the trilinear-related coupling terms between the two phases leads to the phase transition at under tensile strain and the strong competing of the AFD contribution drives the phase transition under compressive strain.

Finally, the strain tunable trilinear-related coupling terms in the two phases play an important role in inducing the phase transitions at both compressive and tensile strains. Although this unusual P-NP transition was discovered in $Ca_3Ti_2O_7$ compound, it is general and can be applied to other compounds in the $A_3B_2O_7$ family [27]. By using the tolerance factor as a descriptor, it was shown that compounds with small tolerance factors, and thus having strong OOR and OOT modes, should exhibit two nonpolar phases (one occurring under each compressive and tensile strains, respectively, see **Table 1**). With increasing tolerance factor, there will be only one nonpolar phase under compressive strain. In this scenario with increasing tolerance factor, the nonpolar phase transforms from *Pbcn* to *Ccca* with only the OOR mode present on the compressive side and it transforms from *Pbcn* to $P4_2/mnm$ with only the OOT mode on the tensile side. The change in symmetry of the nonpolar phase is attributed to the strain-oxygen octahedral rotation coupling, in which compressive strain favors the OOR and tensile strain favors the OOT, thus leading to the appearance of the *Ccca* phase at compressive strains and the $P4_2/mnm$ phase at tensile strains with additional instability of the oxygen octahedral rotations at large tolerance factor.

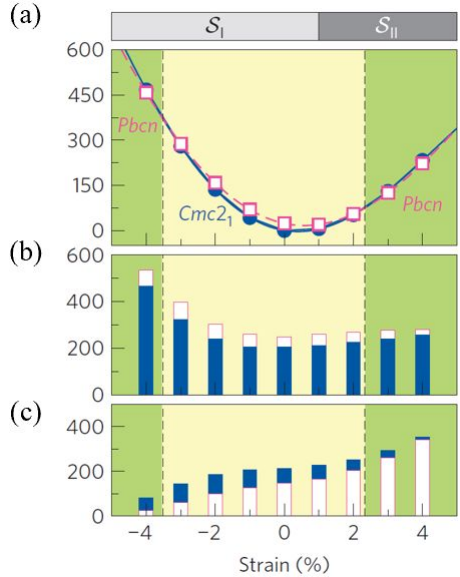

Figure 4. (a) Stability of the *Cmc*2_1 and *Pbcn* phases with strain based on the Landau phenomenological model. (b), (c) Energy contributions from the AFD (b) and FE(AFE)–AFD (c) interaction terms to the energy gains with respect to the *I*4/*mmm* structure for each *Cmc*2_1 and *Pbcn* phase, respectively, with strain. Figures reproduced from Ref. 16, Copyright Springer Nature, 2016.

Table 1. Calculated tolerance factors obtained using the bond valence model (τ_1) and crystal ionic radii presented in Ref. [36] (τ_2), respectively, for layered oxides exhibiting P-NP transitions in thin films. The cross indicates there is no tensile NP phase appearing. P_C and P_T are polarizations in unit of $\mu C/cm^2$ in the polar phase (i.e., *Cmc*2_1) near the compressive and tensile P-NP transition boundaries, respectively, which are at -3 and 3%, -2 and 2%, -2 and 2%, -2%, -2% with increasing tolerance factor.

	$Ca_3Ti_2O_7$	$Sr_3Zr_2O_7$	$Sr_3Sn_2O_7$	$Ca_3Mn_2O_7$	$Ca_3Ge_2O_7$
Compressive NP Symmetry	*Pbcn*	*Pbcn*	*Pbcn*	*Ccca*	*Ccca*
Tensile NP Symmetry	*Pbcn*	*P*4_2/*mnm*	*P*4_2/*mnm*	×	×
P_C	5.7	4.8	3.6	3.2	3.0
P_T	36.5	9.5	8.8	×	×
τ_1	0.946	0.946	0.957	0.979	0.980
τ_2	0.846	0.861	0.873	0.879	0.879

Beyond single B-site transition metal $A_3B_2O_7$ compounds, there are B-site ordered $A_3BB'O_7$ compounds possessing similar phase transitions in (001) oriented films. These materials exhibit homogenous layers of B^{4+} cations that alternate with layers of B'^{4+} cations in the perovskite block in the [001] direction [27] (see **Figure 5a**). But at the phase transition, the disappearance of ferroelectricity only occurs in the *in*-plane orientation, because the out-of-plane polarization is constrained by symmetry due to the broken mirror-plane symmetry operation perpendicular to the (001) plane. Owing to this symmetry constraint, the lower-energy *Cmc*2_1, *Pbcn* and *Ccca* phases in the pure $A_3B_2O_7$ compounds become the *Cc*, *Pna*2_1 and *Aba*2 phases in the B-site ordered compounds, respectively (see **Figures 5b** and **5c**). Besides the new *out-of-plane* polarization along the [001] direction, the other phonon modes present in the three phases of ordered $A_3BB'O_7$ are essential similar to those in the pure compounds. The disappearance of the *in-plane* polarization was then demonstrated in the $Ca_3(Ti,B')_2O_7$ (*B*'=Mn,Tc) compounds, where the phase transition was transformed from *Cc* to *Pna*2_1 under tensile strain. At this transition, the *out-of-phase* OOR transforms to an *in-phase* OOR. Therefore, by intercalating two $A_3B_2O_7$ compounds to construct a B-site ordered $A_3BB'O_7$ compound, one can also achieve on/off switching of the polarization at the *Cc*-*Pna*2_1 phase transition.

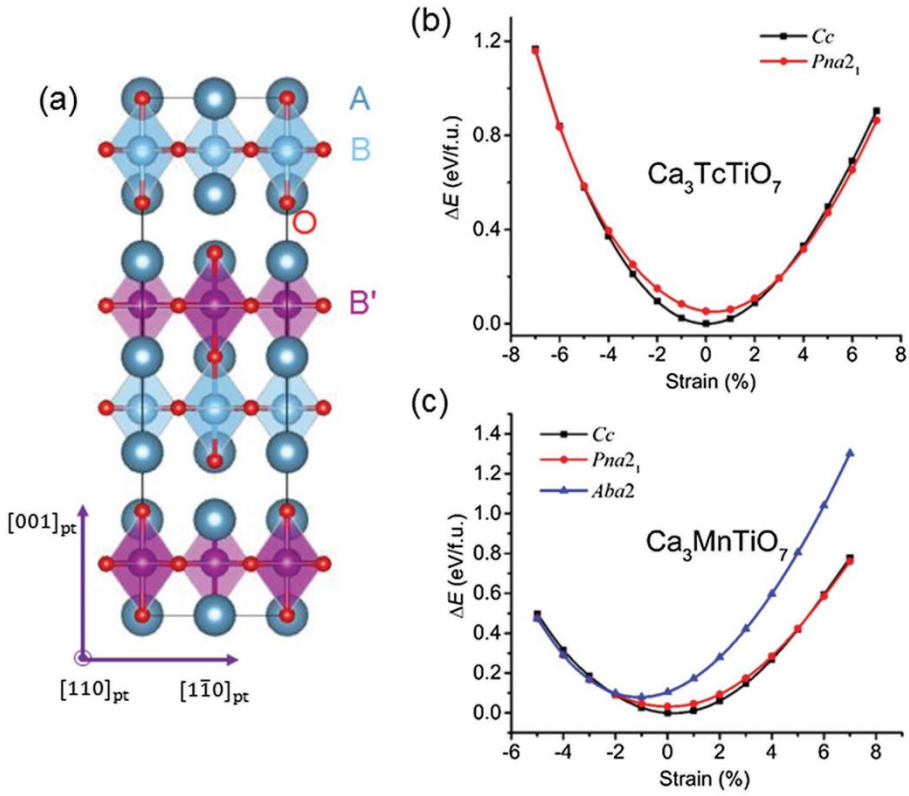

Figure 5. (a) Illustration of the layered (001) B-cation order in the Ruddlesden-Popper $A_3BB'O_7$ compound. The high symmetry structure, which adopts *I*4/*mmm* symmetry before substitution, undergoes a symmetry reduction to *I*4*mm* symmetry after substitution. The epitaxial plane is the (001) plane. (b) and (c) show the calculated total energies as a function of biaxial strain for Ca_3TcTiO_7 and Ca_3MnTiO_7, respectively, where the energy is given relative to that of the *Cc* phase at 0% strain. Figures reproduced from Ref. 27, Copyright WILEY-VCH Verlag GmbH & Co. KGaA, Weinheim, 2017.

HYBRID IMPROPER ANTIFERROELECTRIC *P*4$_2$/*mnm* PHASE

The *P*4$_2$/*mnm* can also be an antiferroelectric phase, since it has symmophic polar subgroups *Cmm*2 and *Cm* that can preserve the polar site symmetries of *P*4$_2$/*mnm* (i.e., *mm*2 and *m*). This phase is also hybrid improper antiferroelectric, due to the fact that the antiferroelectric M_2^+ mode condenses in the *P*4$_2$/*mnm* phase because the X_3^- OOR mode couples through odd-order terms (**see Figure 6**) [16]. This *P*4$_2$/*mnm* phase is found in tensile strained $Sr_3Zr_2O_7$ and $Sr_3Sn_2O_7$ film, as shown in **Table 1**. Thus, a P-NP phase transition was predicted involving the transformation from *Cmc*2$_1$ to *P*4$_2$/*mnm* (see **Table 1**).

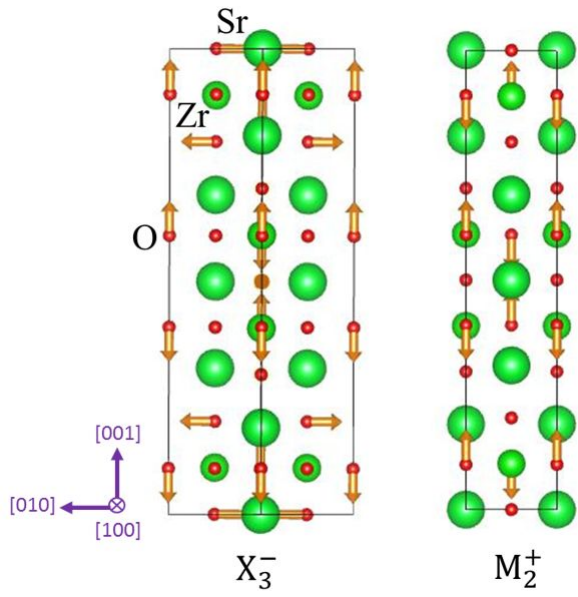

Figure 6. The X_3^- and M_2^+ modes appearing in the $P4_2/mnm$ phase. The yellow arrows indicate the atomic displacement directions. Figures reproduced from Ref. 16, Copyright Springer Nature, 2016.

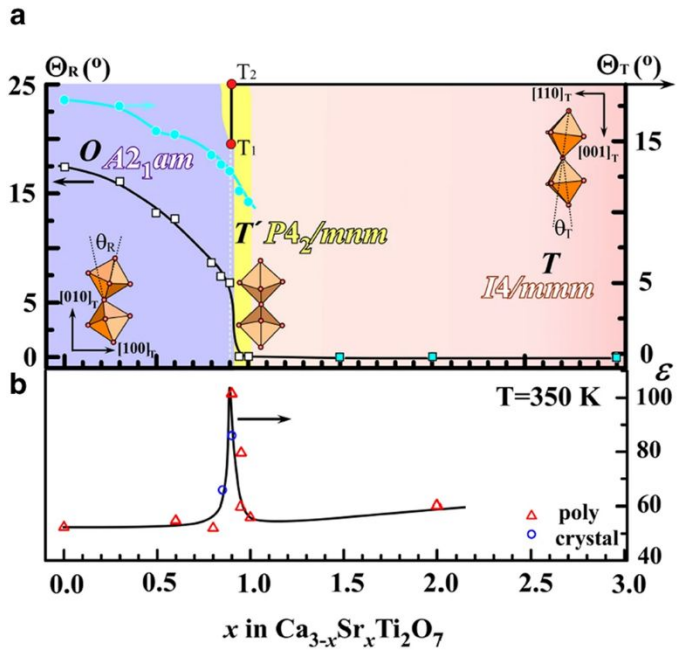

Figure 7. (a) Structural phase diagram of $Ca_{3-x}Sr_xTi_2O_7$ parameterized in terms of the angles of octahedral rotation (Θ_R, empty squares) and tilt (Θ_T, cyan circles) by varying Sr composition, x. (b) Dielectric constant as a function of Sr composition, x, measured at 350 K and 44 kHz. The dielectric constant peak occurs at the $A2_1am$- $P4_2/mnm$ boundary of x=0.9. Figures reproduced from Ref. 37, Copyright Springer Nature, 2016.

In a study of Sr substituted $Ca_3Ti_2O_7$, i.e., $Ca_{3-x}Sr_xTi_2O_7$, *in situ* heating transmission electron microscopy (TEM) studies [37], synchrotron powder X-ray diffraction experiments and dielectric measurements (**Figure 7**), showed that a $P4_2/mnm$ phase can occurs at x=0.915-1 and T= 473-710 K, upon varying the Sr composition (x) and temperature (T). The $P4_2/mnm$ appears as an intermediate phase between the $Cmc2_1$ and $I4/mmm$ phases, which are the low-temperature ground state and high-temperature equilibrium phases, respectively. Furthermore, there is a change of dielectric constant about 40 across the phase transition from $Cmc2_1$ to $P4_2/mnm$ [See **Figure 7(b)**] which is consistent with our prediction that there will be a change of dielectric constant across the P-NP phase transition in $Ca_3Ti_2O_7$, as will be discussed in the section of "**Tunable dielectric response**".

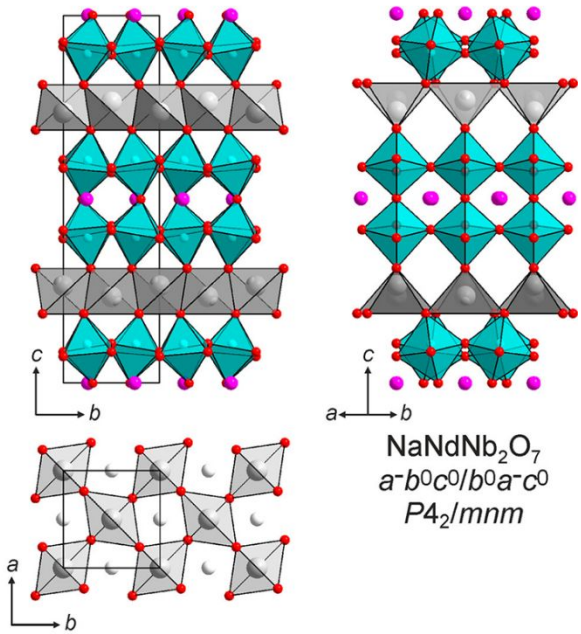

Figure 8. Structures of $NaNdNb_2O_7$. Purple, blue, light-gray, and red spheres represent Nd, Nb, Na, and O, respectively. This structure was obtained through cation-exchange reactions performed on the n = 2 Dion–Jacobson phase $RbNdNb_2O_7$, using $NaNO_3$. Figure reproduced from Ref. 38, Copyright © 2018 American Chemical Society.

In the $NaNdM_2O_7$ (M = Nb, Ta) layered-perovskite-like structures (**Figure 8**) [38], synchrotron X-ray and neutron powder diffraction data led to identification of the

$P4_2/mnm$ phase as the ground state structure. In this case, it arises from the requirement to minimize the Na−Na repulsion. Furthermore, the authors proposed that the competition between minimizing the A′-A′ repulsion and optimizing the A′-cation coordination environment may be used as a guideline for choosing the A′=cation to find additional antiferroelectric phases in $A'AB_2O_7$ structures. As discussed in the $P4_2/mnm$ phase of $A_3B_2O_7$ compounds, here, the $P4_2/mnm$ phase may be antiferroelectric according to the symmetry analysis. But whether it is also hybrid improper antiferroelectric as in $A_3B_2O_7$, this can be solved by using first-principles calculations in the future studies.

THE ANTIFERROELECTRIC *C*2/*c* PHASE

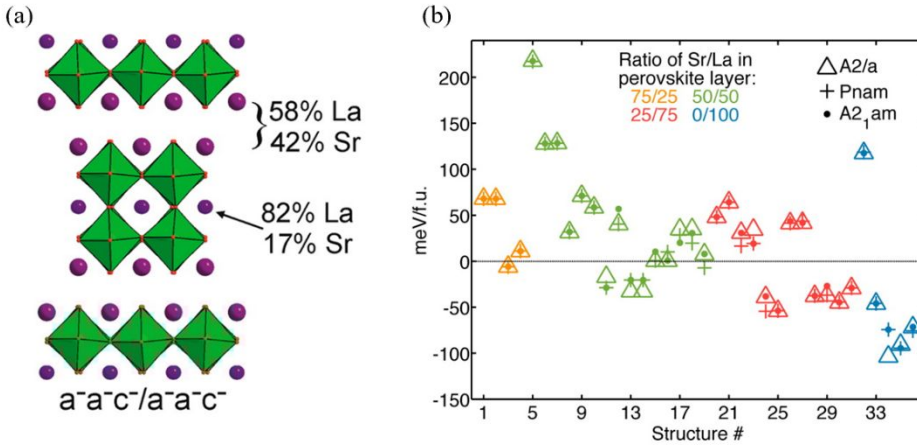

Figure 9. The structure of the $La_2SrCr_2O_7$ Ruddlesden−Popper structure with small in-plane out-of-phase tilts (Glazer notation: $a^-a^-c^0$) and out-of-plane out-of-phase rotations ($a^0a^0c^-$) shown. (b) Energy of the *C*2/*c* (alternative setting, *A*2/*a*), *Pnma* (*Pnam*) and $Cmc2_1$ ($A2_1am$) with varying La/Sr distributions. Figures reproduced from Ref. 39, Copyright © 2016 American Chemical Society.

$La_2SrCr_2O_7$ was synthesized in the Ruddlesden−Popper structure [see **Figure 9(a)**] [39] and neutron diffraction measurements showed that the *C*2/*c* symmetry is its ground state symmetry [**Figure 9(b)**]. Although no investigations in the literature showed that it is a hybrid improper antiferroelectric phase, the *C*2/*c* symmetry follows the aforementioned space-group requirements for assessing antiferroelectricity. This is because in *C*2/*c* phase, there is a polar site "1", which can preserve a symmorphic polar subgroup of the *C*2/*c* phase, that is, the *P*1 phase. Besides, the *C*2/*c* phase has the same Glazer notation of $a^-a^-c^-$ about the OOT and OOR modes as those in *Pbcn*.

Therefore, performing A-site or B-site cation substitution in the *n*=2 Ruddlesden−Popper compounds can be a useful route to achieve a complex temperature-dependent phase diagram that may exhibit an antiferroelectric ground state or intermediate equilibrium phase over a finite temperature range, such as those found in the above compounds and in $Sr_2(Ho,Y)Mn_2O_7$ [40] and $Tb_2Sr(Fe,Co)_2O_7$ [41-43].

Although the antiferroelectric phase does not exhibit a functional polarization, it is still useful, as described next.

FUNCTIONALITIES AT THE P-NP PHASE TRANSITION

1. Tunable dielectric response

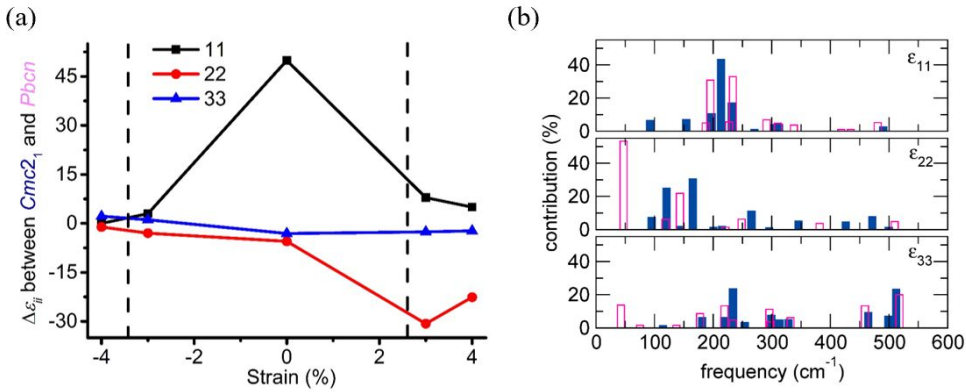

Figure 10. (a) The calculated relaxed-ion ($\Delta\epsilon_{ij}$, ij=11, 22, 33) dielectric tensors for the $Cmc2_1$ and *Pbcn* phases in $Ca_3Ti_2O_7$ at selected strains. Since the $Cmc2_1$ and *Pbcn* phases belong to the 2*mm* and *mmm* point groups, respectively, there are only three independent coefficients ($\epsilon_{11} \neq \epsilon_{22} \neq \epsilon_{33}$) for the two phases. (b) The contribution from each phonon mode to the ionic part of the dielectric constant in each direction at 3% strain in $Cmc2_1$ (solid blue bar) and *Pbcn* (opened pink bar) phases. Figures reproduced from Ref. 16, Copyright Springer Nature, 2016.

Phase transitions are usually accompanied by changes in physical properties. Here, a large difference of approximately ~30 in the dielectric constant ε_{22} along the polarization direction (i.e., *b* direction) under tensile strain was found in $Ca_3Ti_2O_7$ by using DFT-PBEsol calculations [16] as shown in **Figure 10a**. After decomposing the dielectric constants into contributions from the infrared active modes, it was identified that a very low-frequency mode, which contributes to the dielectric constant in the *b* direction in the *Pbcn* phase, induces the large difference of the dielectric constant between the two phases around 3% strain. This low-frequency mode does not occur in the same range in the $Cmc2_1$ phase (**Figure 10b**). In experiment, there is indeed a change of dielectric constant (~40) at the boundary between the polar $Cmc2_1$ phase to the hybrid improper antiferroelectric $P4_2/mnm$ phase in bulk $Ca_{3-x}Sr_xTi_2O_7$ (x=0.9), as shown in **Figure 7(b)**.

2. Alternative way to tune weak ferromagnetism in $A_3B_2O_7$

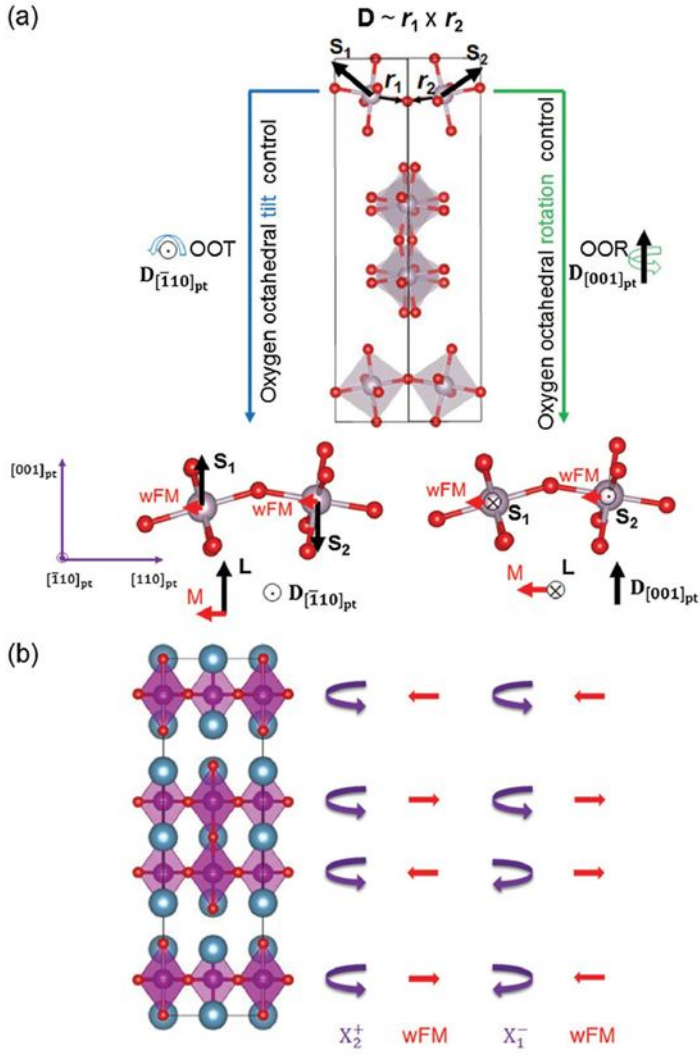

Figure 11. (a) Mechanisms for oxygen octahedral tilt (left, blue) and rotation (right, green) control of weak ferromagnetism. S_i (i=1,2), D_i (i=1,2), r_i (i=1,2), **M** and **L** represent the local spin vectors, DM-interaction vectors, unit vectors along the S_i-O bond direction, and the wFM and AFM vectors, respectively. The polar $Cmc2_1$ structure (center) is shown as reference without the A cations for clarity along with the pseudotetragonal axes. (b) Illustration of how the wFM vector changes upon reversing the sense of the OOR in the perovskite block of the $A_3B_2O_7$ Ruddlesden-Popper $I4/mmm$ structure through the X_2^+ (i.e., OOR in $Cmc2_1$) and X_1^- (i.e., OOR in $Pbcn$) modes. Purple arrowed arcs indicate the BO_6 rotation sense in each perovskite layer. Red arrows indicate the direction of the wFM. Note that the net magnetization is always zero in both cases. Figures reproduced from Ref. 27, Copyright WILEY-VCH Verlag GmbH & Co. KGaA, Weinheim, 2017.

The n=2 RP $Ca_3Mn_2O_7$ exhibits a novel magnetoelectric (ME) coupling mechanism [17], where the ground magnetic structure adopts G-type spin order with the spins along the $[001]_{pt}$ direction and a weak ferromagnetic spin canting along the $[110]_{pt}$ direction as shown in the left panel of **Figure 11a**. The spins point along the

$[001]_{pt}$ direction because of the spin anisotropy, whereas the weak ferromagnetism (wFM) results from the Dzyaloshinskii–Moriya (DM) interaction, which has an energy contribution expressed as $E_{DM} = \mathbf{D} \cdot (\mathbf{L} \times \mathbf{M})$ where **D**, **L** and **M** are the DM interaction vector, antiferromagnetic (AFM) vector $\mathbf{L}=\mathbf{S}_1-\mathbf{S}_2$, and the wFM vector $\mathbf{M}=\mathbf{S}_1+\mathbf{S}_2$, respectively. The **D** vector is also proportional to approximately $\boldsymbol{r_1} \times \boldsymbol{r_2}$, where $\boldsymbol{r_1}$ and $\boldsymbol{r_2}$ are the distance vectors defining the Mn-O bonds in the Mn-O-Mn subsystem as shown in **Figure 11a**. It is then readily found by the right-hand rule that the DM vector induced by OOT can produce wFM according to E_{DM} expression, which is along the direction perpendicular to both **D** and **L** vectors (**Figure 11a**, **left panel**). In contrast, the DM vector induced by OOR is in the same direction as **L**, which leads to a zero E_{DM} and no weak ferromagnetism. This tilt-control mechanism leads to on/off-control of wFM. Therefore, if an external electric field switches the direction of the polarization, then either OOR or OOT will be reversed due to the trilinear coupling interaction. Whether the rotation or tilt mode switches is mainly determined according to which switching path has the lower energy barrier [42]. If the polarization switching favors switching of the OOT, then the direction of the wFM will switch simultaneously because of the reversal of $\mathbf{D} \sim \boldsymbol{r_1} \times \boldsymbol{r_2}$, which corresponds to the octahedral tilt control route as shown in the bottom left panel of **Figure 11a**.

In recent work using DFT-PBEsol calculations [27], it was shown that an alternative promising route to realize electric-field controllable magnetism at room temperature in multiferroics can occur based on the family of $A_3B_2O_7$ layered perovskites. In $Ca_3Mn_2O_7$, when the magnetic anisotropy is in-plane, as in the tensile regime of (001) $Ca_3Mn_2O_7$ films, then control of wFM by OOT is not possible. Another mechanism for control of wFM becomes active where the direction of the wFM is determined by the OOR. This is because the wFM direction is oriented in in-plane when the magnetic anisotropy is also in-plane and is induced by the *out-of-plane* DM interaction. The direction of the *out-of-plane* DM interaction is further controlled by the OOR mode (**Figure 11a**, **right panel**). However, although though the direction of wFM can be switched at the P-NP phase transition due to the change of OOR mode pattern, there will be no net wFM in both phases (**Figure 11b**).

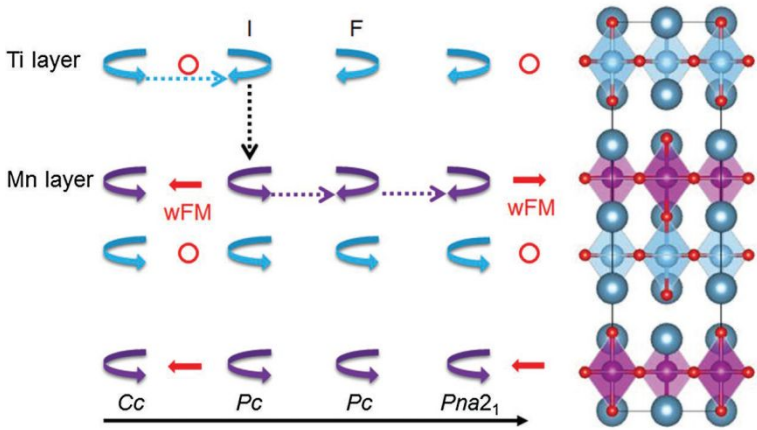

Figure 12. Illustration of the two-step transformation process by OOR at the *Cc*-*Pna*2_1 phase boundary in Ca_3MnTiO_7. I and F indicate the initial step and final step in the switching process from the polar *Cc* (left, with both in- and out-of-plane polarization) phase to the polar *Pna*2_1 (right, with only out-of-plane polarization) phase through the polar *Pc* intermediate structure. The blue and purple arrowed arcs indicate the BO_6 rotation sense in Ti and Mn perovskite layers, respectively. Red open circles and arrows indicate no wFM in Ti perovskite layers and the direction and magnitude of

wFM in Mn perovskite layers, respectively. Dashed arrows track the layers in which the sense of OOR change during the process. Figure reproduced from Ref. 27, Copyright WILEY-VCH Verlag GmbH & Co. KGaA, Weinheim, 2017.

Interestingly, in magnetic $A_3BB'O_7$ films, the OOR control of the wFM is still active when the magnetic anisotropy is oriented *in-plane* and there will be the finite wFM in the *Cc* phase and no wFM in the *Pna*2_1 phase, thus leading to a control of macroscopic magnetism by ferroelectricity across *Cc*-*Pna*2_1 phase transition (**Figure 12**). It was then predicted with DFT-PBEsol calculations that the cation ordered multiferroic Ca_3TcTiO_7 may be a viable candidate exhibiting a switching-path independent room-temperature electric-field controllable magnetism. Although it was recognized these compounds may require care during experimental synthesis owing to radioactivity of technetium the simulations showed that the *Cc*-*Pna*2_1 phase transition occurs at a tensile strain of approximately 3% and the magnetic transition temperature can be as high as ~358K at 3% strain from a Monte Carlo simulation.

ANTIFERROELECTRIC PHASES AND DOMAIN WALLS IN $A_3B_2O_7$

Table 2. Summary of switching paths in 180° domain walls of $A_3B_2O_7$. Data in the table is from Ref. 44.

Path	Barrier	Intermediate phase	$E_{barrier}$ (meV/Ti)
One step	*Cmcm*		56
One step	*Cmca*		90
Two step	*Pmc*2_1	*Pnma*	32
Two step	*Pmn*2_1	*Pnma*	35
Two step	*Cmm*2	*Cmc*2_1	41

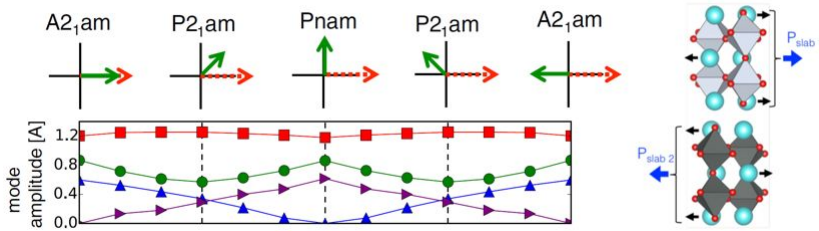

Figure 13. Two step polarization switching path with the intermediate phase as *Pnma*. Red arrow and square represent the OOT mode ($Q_{X_3^-}$) and the green arrow and circle represent the OOR mode ($Q_{X_2^+}$). Blue triangles represent the ferroelectric mode ($Q_{\Gamma_5^-}$) and purple triangles represent the antiferroelectric mode. The evolution of the (top panel) mode direction and (bottom panel) mode amplitude in the transition path. The antiferroelectric mode is also shown. The other modes can be found in Figure 3. Figures reproduced from Ref. 44, Copyright American Physical Society, 2016.

In a study of the domain wall structure of $Ca_3Ti_2O_7$ [44], the authors showed an intermediate *Pnma* phase occurs by using first principles calculations (see **Figure 13**) as the polarization switches from one orientation to its opposite (180°) orientation. The *Pnma* phase can be regarded as antiferroelectric phase, because there is a polar site "1" that preserves the symmorphic P*1* subgroup of the *Pnma* phase. This *Pnma* phase helps in understanding how polarization switching occurs across the 180° domain wall, because the possible behavior of the polarization in the switching path can be determined, in which the intermediate phase must lead to a low energy barrier (**Table 2**).

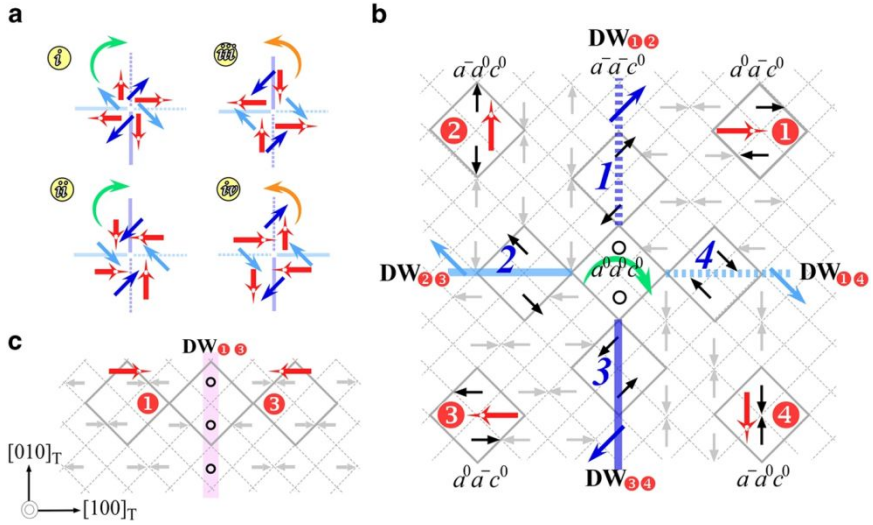

Figure 14. (a) Z_4 vortex (*i* and *ii*) and antivortex (*iii* and *iv*), where the red arrow indicates the OOT mode direction in the domain, and the blue and light blue arrows indicate the mode direction in the domain wall (DW). The green and orange arrows indicate the vortex and antivortex, respectively. (b) Z_4 vortex in (i) of Figure (a). (c) The DW formed by domains 1 and 3. Figures reproduced from Ref. 37, Copyright Springer Nature, 2016.

In another study of the vortex-antivortex in the domain and domain wall of $Ca_{3-x}Sr_xTi_2O_7$ [37], a new type of Z_4 vortex-antivortex was found in the $P4_2/mnm$ phase (x=0.95) [see **Figure 14(a)**], while a type of Z_3 vortex-antivortex was found in the $Cmc2_1$ phase in an earlier study from the same research group (x<0.5) [24]. The Z_4 vortex-antivortex is led by the tilt mode (OOT) and it can only result in four domains [**Figure 14(a)**]. The Z_3 vortex-antivortex results from the tilt (OOT), rotation (OOR) and polar modes, which permits then the formation of eight domains. As discussed in the domain walls of the Z_3 vortex-antivortex, there are many charged domain walls that may leading to variable conductance [24]. Therefore, the hybrid improper $P4_2/mnm$ phase may be a new platform to explore similar functionalities as in the $Cmc2_1$ phase in $Ca_{3-x}Sr_xTi_2O_7$. Furthermore, the OOT distortion in $P4_2/mnm$ phase is similar to that in $La_{2-x}Ba_xCuO_4$ which hosts superconductivity [45]; thus, the $P4_2/mnm$ phase may also enrich the functionalities in the n=2 Ruddlesden–Popper compounds upon hole- or electron doping.

PERSPECTIVES ON THE HYBRID IMPROPER ANTIFERROELECTRICS

Many studies focused on antiferroelectric transitions have been reported, including in inorganic oxides [6,7] (e.g., $PbZrO_3$, $AgNbO_3$, $PbHfO_3$ etc.), orthorhombic *ABC* semiconductors [9] (e.g., MgSrSi), hydrogen-bonded organic compounds [10-13] (e.g., $NH_4H_2PO_4$, NH_4HSO_4, 2-trifluoromethylbenzimidazole, etc.), hybrid inorganic−organic framework with the perovskite architecture [46,47] and

antiferroelectric Aurivillius compound [48]. Recently, the hybrid improper (anti)ferroelectrics were proposed and demonstrated in both theory and experiments [16,17,28,29,49-51], where the antiferroelectric transition can occur above room temperature [28,29,50]. Beyond hybrid improper antiferroelectricity occurring in $A_3B_2O_7$ compounds, this behavior was also predicted in $ABO_3/A'BO_3$ and $AA'BB'O_6$ compounds [30].

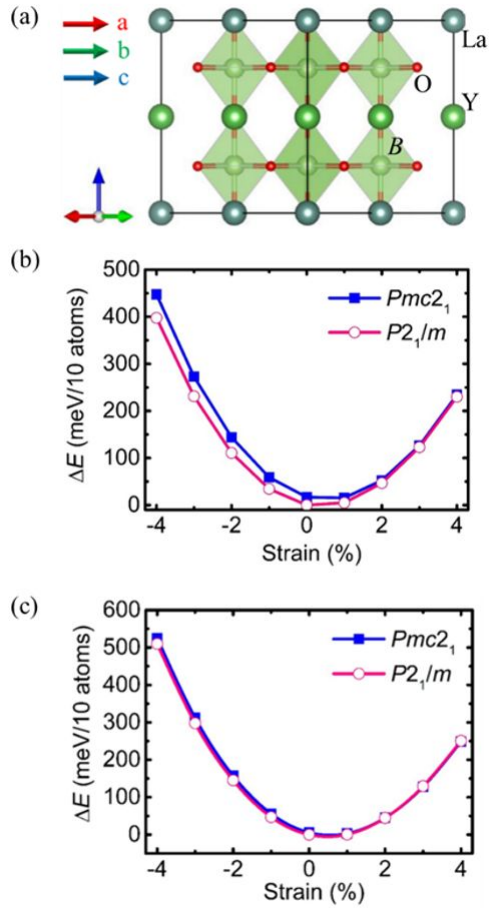

Figure 15. (a) Schematic La*B*O_3/Y*B*O_3 (*B* = Al, Ga) superlattice structure. Calculated total energies as a function of biaxial strain, where the energy is given relative to that of the *P*21/*m* phase at 0% strain in (b) $LaGaO_3/YGaO_3$ and (c) $LaAlO_3/YAlO_3$, respectively. Figures reproduced from Ref. 30, Copyright American Physical Society, 2018.

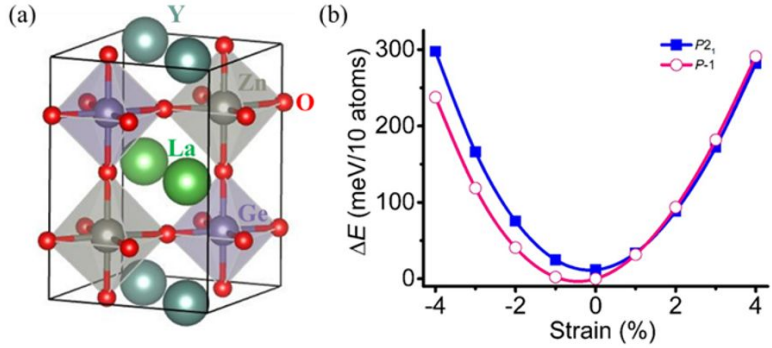

Figure 16. (a) Double perovskite AA′BB′O_6 in *P*4/*nmm* symmetry with layered (001) ordering of A-site cations and rock-salt (111) ordering of B-site cations. (b) Calculated total energies as a function of biaxial strain for LaYZnGeO_6, where the energy is given relative to that of the $P\bar{1}$ phase at 0% strain. Figures reproduced from Ref. 30, Copyright American Physical Society, 2018.

It was demonstrated that the polar-nonpolar transition can also be found in La*B*O_3/Y*B*O_3 (*B* = Al, Ga) superlattices (see **Figure 15**) and La*A*ZnGeO_6 (*A* = Gd, Y, Lu) double perovskites (**Figure 16**) under (001) biaxial strain [30] by using DFT-PBEsol calculations. The phase transition from $P2_1/m$ to $Pmc2_1$ occurs at approximately 2% strain in $LaAlO_3/YAlO_3$ and at an even larger strain in $LaGaO_3/YGaO_3$. In LaYZnGeO_6, the phase transition from $P\bar{1}$ to $P2_1$ is near 1% strain. The reason for the P-NP transition can also be attributed to a strain tunable trilinear-related coupling in the polar, $Pmc2_1$, and nonpolar, $P2_1/m$, structures [30].

This transition can be exploited for optical gap control shown for $LaGaO_3/YGaO_3$ (**Figure 17**). Upon the P-NP phase transition, there is an interesting direct-to-indirect band gap transition, where the polar $Pmc2_1$ exhibits an indirect band gap and the nonpolar $P2_1/m$ phase exhibits a direct band gap (**Figure 17a**). Analysis of the oxygen-oxygen (i.e., *p*-*p*) orbital interactions and the oxygen-transition metal (i.e., *p*-*d*) orbital interactions leads to a competition that induces the direct-to-indirect band gap transition (see **Figure 17b**). The *p*-*d* orbital interactions dominate over the *p*-*p* orbital interactions to give the indirect band gap whereas the *p*-*p* orbital interactions dominate over *p*-*d* orbital interactions in the direct band gap configuration (**Figure 17c**). These orbital interactions are tuned by strain and oxygen octahedral rotational modes, in which the large oxygen octahedral rotations and small tensile strain favor the indirect band gap. The above theory of the indirect-direct band gap transition was also applied to La*A*ZnGeO_6 (*A* = Gd, Y, Lu) double perovskites. This provides a way to engineering the indirect-direct band gap transition in the three dimensional oxides, while indirect-direct band gap transitions occur more frequently in ultrathin silicon films [52,53] and transition metal dichalcogenides [54,55].

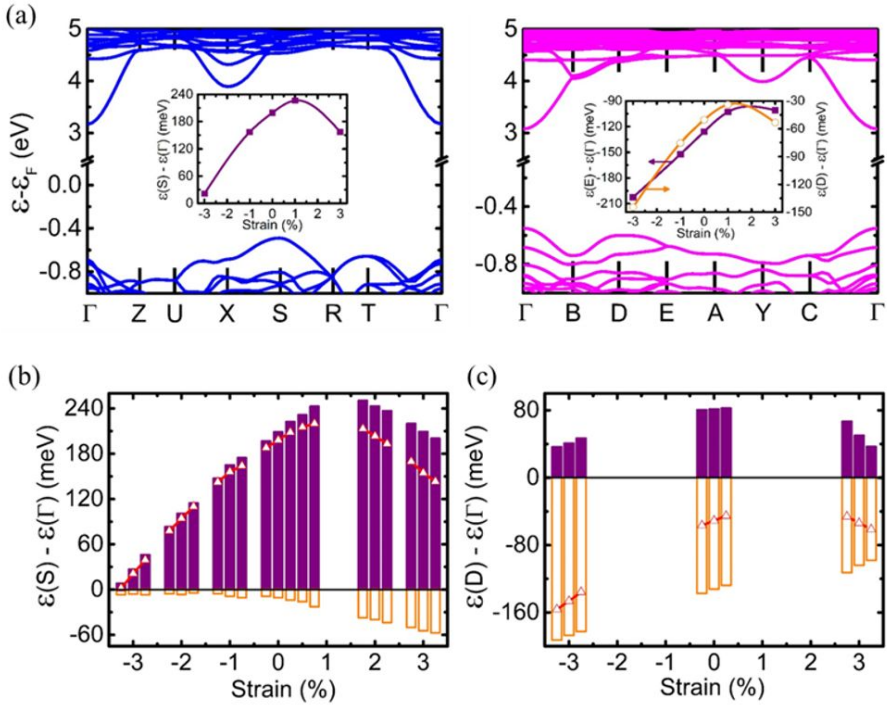

Figure 17. (a) Band structures for the polar $Pmc2_1$ (left panel) and nonpolar $P2_1/m$ (right panel) phases at 0% strain in $LaGaO_3/YGaO_3$. The insets in (a) show the dependence of the valence band eigen-energy differences, $\Delta\varepsilon_{S-\Gamma}$, $\Delta\varepsilon_{E-\Gamma}$, and $\Delta\varepsilon_{D-\Gamma}$, with strain., Decomposition of (b) $\Delta\varepsilon_{S-\Gamma}$ in $Pmc2_1$ and (c) $\Delta\varepsilon_{D-\Gamma}$ in $P2_1/m$, respectively, into energy contributions from the O-*p*...O-*p* and O-*p*...X interactions in $LaGaO_3/YGaO_3$. The solid (open) bars indicate the part from the O-*p*...X (O-*p*...O-*p*) interaction. The open triangles and solid red lines show the net effects by summing energy contributions from the O-*p*...O-*p* and O-*p*...X interactions. Figures reproduced from Ref. 30, Copyright American Physical Society, 2018.

Recently, several experiments have also demonstrated competing hybrid improper ferroelectric phases at high temperature in bulk $Sr_3Zr_2O_7$ [28], $Sr_3Sn_2O_7$ [29], $Li_2SrNb_2O_7$ [49] and in organic-inorganic $((CH_3)_2CHCH_2NH_3)_2CsPb_2Br_7$ [50] compounds. In $Sr_3Zr_2O_7$ and $Sr_3Sn_2O_7$, the ground state phase is similar to that in $Ca_3Ti_2O_7$. It is the polar $Cmc2_1$ phase, i.e., $A2_1am$ as shown in **Figure 18** using a different crystallographic setting, therefore, both compounds are also hybrid improper ferroelectrics in bulk. However, upon increasing the temperature to ~400 K and ~600 K (**Figures 18a** and **18b**), the hybrid improper antiferroelectric *Pbcn* phase (i.e., *Pnab* phase in **Figure 18**) appeared in $Sr_3Sn_2O_7$ and $Sr_3Zr_2O_7$, respectively. The experimental Curie temperature in $Sr_3Sn_2O_7$ can be tuned by a small amount of Ca substitution at A site. The hybrid improper antiferroelectricity was also demonstrated using symmetry arguments and calculations based on density functional theory in both materials.

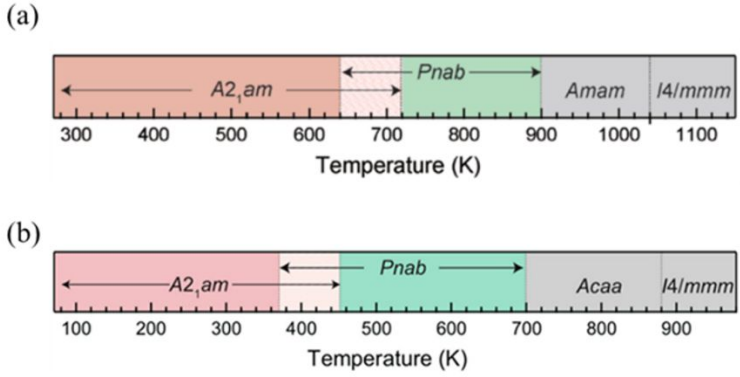

Figure 18. Sequence of polymorphic transitions in (a) $Sr_3Zr_2O_7$ and (b) $Sr_3Sn_2O_7$, respectively. Figure (a) reproduced from Ref. 28, Copyright WILEY-VCH Verlag GmbH & Co. KGaA, Weinheim, 2018; Figure (b) reproduced from Ref. 29, Copyright © 2018 American Chemical Society.

In the n=2 RP $Li_2SrNb_2O_7$, the ground state *Pnma* phase was demonstrated to be a hybrid improper antiferroelectric. Upon increasing the temperature to ~200 K, there will be a hybrid improper ferroelectric $Cmc2_1$ phase stablized. At 77 K, a hybrid improper antiferroelectric-ferroelectric phase transition occurs and a double hysteresis loop was obtained (**Figure 19a**). The antiferroelectric *Pnma* phase was also observed in the two-dimensional Ruddlesden−Popper $((CH_3)_2CHCH_2NH_3)_2CsPb_2Br_7$ comprising the complex isobutylammonium and Cs cations on the A site, while its hybrid improper antiferroelectric feature should be investigated in the future. The phase transition to *Pnma* phase was reported to be above room temperature (~353 K) and attributed to the synergistic dynamic motion of the inorganic Cs atoms and organic isobutylammonium cations (**Figure 19b**). At room temperature, a clear double hysteresis loop was demonstrated and maintained from 298 K to 353 K (**Figure 19c**). The energy storage efficiency, up to 69% at 94 kV/cm, achieved in this compound is also comparable to other proper antiferroelectrics.

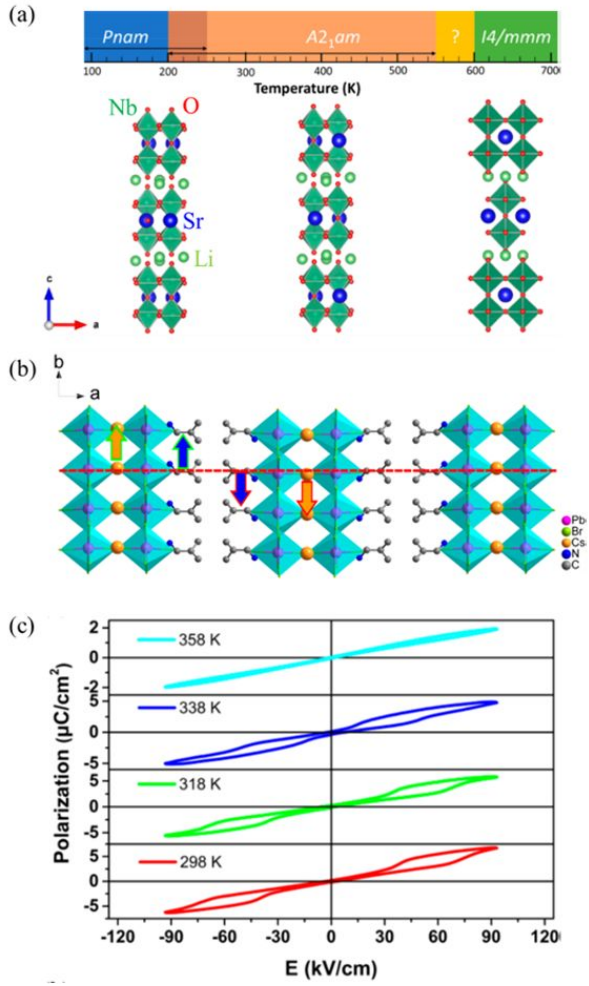

Figure 19. (a) The phase transition sequence and change in crystallographic symmetry for $Li_2SrNb_2O_7$. (b) The nonpolar *Pnma* phase of $((CH_3)_2CHCH_2NH_3)_2CsPb_2Br_7$. The arrows indicate the synergistic dynamic motion of inorganic Cs atoms and organic isobutylammonium cations. (c) Double hysteresis loop in a wide temperature range. Figure (a) reproduced from Ref. 49, Copyright © 2019 American Chemical Society; Figures (b) and (c) reproduced from Ref. 50, Copyright © 2019 American Chemical Society.

SUMMARY

We have described several important works on advancing an understanding of hybrid improper antiferroelectrcity, which initiated from first-principles calculations and more recently has spawned experimentation. with a focus on above-room-temperature hybrid improper for potential electronic applications. These compounds may serve in energy storage applications, as an enhancement of $\int PdE$, where the P and E are polarization and electric field, respectively, is enabled by the shape of the double hysteresis loop possessed by an anitferroelectric [5]. The stored energy can be roughly

twice of that of a linear dielectric with the same polarization at a field above the transition field. There are also changes in physical properties at the hybrid improper ferroelectric-antiferroelectric transition, such as, the tunable dielectric constant for the microwave devices [16], the tunable wFM for the multiferroic memory devices [27] and tunable indirect-direct band gap for tunable photoluminescence [30]. We believe hybrid improper antiferroelectricity provides a complementary path to realize new antiferroelectrics, which may find use in the applications with novel properties in the future.

ACKNOWLEDGEMENTS

X.-Z.L. and J.M.R. were supported by the National Science Foundation (NSF) through the Pennsylvania State University MRSEC under Award No. DMR-1420620 and DMR-2011208.

References

1. M.E. Lines, A.M. Glass, Principles and Applications of Ferroelectrics and Related Materials, Cambridge University Press (1977).

2. T. Mitsui, Ferroelectrics and antiferroelectrics, in Springer Handbook of Condensed Matter and Materials Data, Part 4, Springer-Verlag, pp. 903–938 (2005).

3. C. Kittel, *Phys. Rev.* **82**, 729 (1951).

4. P. Tolédano, M. Guennou, *Phys. Rev. B* **94**, 014107 (2016).

5. K. M. Rabe, in Functional Metal Oxides: New Science and Novel Applications, edited by S. Ogale and V. Venkateshan, Wiley, New York (2013).

6. H. Liu, B. Dkhil, *J. Kristallogr.* **226**, 163 (2011).

7. X., Tan, C. Ma, J. Fredrick, S. Beckman, K. G. Webber, *J. Am. Ceram. Soc.* **94**, 4091 (2011).

8. H. Unoki, T. Sakudo, *Phys. Rev. Lett.* **38**, 137 (1977).

9. J. W. Bennett, K. F. Garrity, K. M. Rabe, D. Vanderbilt, *Phys. Rev. Lett.* **110**, 017603 (2013).

10. I. N. Flerov, E. A. Mikhaleva, *Phys. Solid State* **50**, 478−484 (2008).

11. J. Lasave, S. Koval, N. S. Dalal, R. L. Migoni, *Phys. Rev. Lett.* **98**, 267601 (2007).

12. K. Kobayashi, S. Horiuchi, S. Ishibashi, Y. Murakami, R. Kumai, *J. Am. Chem. Soc.* **140**, 3842−3845 (2018).

13. S. Horiuchi, F. Kagawa, K. Hatahara, K. Kobayashi, R. Kumai, Y. Murakami, Y. Tokura, *Nat. Commun.* **3**, 1308 (2012).

14. G. Shirane, E. Sawaguchi, Y. Takagi, *Phys. Rev.* **84**, 476 (1951).

15. W. Känzig, Ferroelectrics and Antiferroelectrics (Academic Press, New York, 1957).

16. X.-Z. Lu, J. M. Rondinelli, *Nat. Mater.* **15**, 951 (2016).

17. N. A. Benedek, C. J. Fennie, *Phys. Rev. Lett.* **106**, 107204 (2011).

18. A.B. Harris, *Phys. Rev. B* **84**, 064116 (2011).

19. N. A. Benedek, A. T. Mulder, C. J. Fennie, *J. Solid State Chem.* **195**, 11 (2012).

20. A. T. Mulder, N. A. Benedek, J. M. Rondinelli, C. J. Fennie, *Adv. Funct. Mater.* **23**, 4810-4820 (2013).

21. N.A. Benedek, J.M. Rondinelli, H. Djani, Ph. Ghosez, P. Lightfoot, *Dalton Trans.* **44**, 10543-10558 (2015).

22. B. B. Van Aken, T. T. M. Palstra, A. Filippetti, N. A. Spaldin, *Nat. Mater.* **3**, 164-170 (2004).

23. E. Bousquet, *et al. Nature* **452**, 732-736 (2008).

24. Y. S. Oh, X. Luo, F.-T. Huang, Y. Wang, S.-W. Cheong, *Nat. Mater.* **14**, 407–413 (2015).

25. M. S. Senn, A. Bombardi, C. A. Murray, C. Vecchini, A. Scherillo, X. Luo, S. W. Cheong, *Phys. Rev. Lett.* **114**, 035701 (2015).

26. X. Q. Liu, J. W. Wu, X. X. Shi, H. J. Zhao, H. Y. Zhou, R. H. Qiu, W. Q. Zhang, X. M. Chen, *Appl. Phys. Lett.* **106**, 202903 (2015).

27. X.-Z. Lu, J. M. Rondinelli, *Adv. Funct. Mater.* **27**, 1604312 (2017).

28. S. Yoshida, *et al*, *Adv. Funct. Mater*. **28**, 1801856 (2018).

29. S. Yoshida, *et al*, *J. Am. Chem. Soc.* **140**, 15690-15700 (2018).

30. X.-Z. Lu, J. M. Rondinelli, *Physical Review Materials* **2**, 054409, (2018).

31. M. J. Pitcher, et al. *Science* **347**, 420-424 (2015).

32. Y. Wang, F.-T. Huang, X. Luo, B. Gao, S.-W. Cheong, 29, 1601288 (2017).

33. D. G. Schlom, *et al. MRS Bull.* **39,** 118-130 (2014).

34. J. M. Rondinelli, S. J. May, J. W. Freeland, *MRS Bulletin* **37**, 261-270 (2012).

35. J. P. Perdew *et al*., *Phys. Rev. Lett.* **100**, 136406 (2008).

36. R. D. Shannon, *Acta Crystallogr. A* **32**, 751 (1976).

37. F.-T. Huang, B. Gao, J.-W. Kim, X. Luo, Y. Wang, M.-W. Chu, C.-K. Chang, H.-S. Sheu and S.-W. Cheong, *npj Quantum Materials* **1**, 16017 (2016).

38. T. Zhu, G. Khalsa, D. M. Havas, A. S. Gibbs, W. Zhang, P. S. Halasyamani, N. A. Benedek and M. A. Hayward, *Chem. Mater.* **30**, 8915-8924 (2018).

39. R. Zhang, B. M. Abbett, G. Read, F. Lang, T. Lancaster, T. T. Tran, P. S. Halasyamani, S. J. Blundell, N. A. Benedek and M. A. Hayward, *Inorg. Chem.* **55**, 8951-8960 (2016).

40. P. D. Battle, J. E. Millburn and M. J. Rosseinsky, *Chem. Mater.* **9**, 3136-3143 (1997).

41. M. Sánchez-Andújar and M. A. Señarís-Rodríguez, *Z. anorg. allg. Chem.* **633**, 1890-1896 (2007).

42. P. J. Hickey, C. S. Knee, P. F. Henry and M. T. Weller, *Phys. Rev. B* **75**, 024113 (2007).

43. D. Samaras, A. Collomb and J. C. Joubert, *J. Solid State Chem.* **7**, 337-348 (1973).

44. E. A. Nowadnick, Craig J. Fennie, *Phys. Rev. B* **94**, 104105 (2016).

45. P. V. Balachandran, D. Puggioni and J. M. Rondinelli, *Inorg. Chem.* **53**, 336-348 (2014).

46. P. Jain, N. S. Dalal, B. H. Toby, H. W. Kroto and A. K. Cheetham, *J. Am. Chem. Soc.* **130**, 32, 10450-10451 (2008).

47. H. L. B. Boström, M. S. Senn and A. L. Goodwin, *Nature Commun*. **9**, 2380 (2018).

48. H. Djani *et al.*, *Phys. Rev. B* **101**, 134113 (2020).

49. R. Uppuluri *et al. Chem. Mater.* **31**, 4418−4425 (2019).

50. Z. Wu *et al. J. Am. Chem. Soc.* **141**, 3812−3816 (2019).

51. N. V. Ter-Oganessian, V. P. Sakhnenko, *J. Phys.: Condens. Matter* **32**, 275401 (2020).

52. T. Cao, D. Wang, D.-S. Geng, L.-M. Liu, J. Zhao, *Phys. Chem. Chem. Phys.* **18**, 7156 (2016).

53. J. Noborisaka, K. Nishiguchi, A. Fujiwara, *Sci. Rep.* **4**, 6950 (2014).

54. N. Lu, H. Guo, L. Li, J. Dai, L. Wang, W.-N. Mei, X. Wu, X. C. Zeng, *Nanoscale* **6**, 2879 (2014).

55. Z. Y. Zhang, M. S. Si, Y. H.Wang, X. P. Gao, D. Sung, S. Hong, J. He, *J. Chem. Phys.* **140**, 174707 (2014).